

In Situ Construction of a LiF-Enriched Interface for Stable All-Solid-State Batteries and its Origin Revealed by Cryo-TEM

Ouwei Sheng, Jianhui Zheng, Zhijin Ju, Chengbin Jin, Yao Wang, Mei Chen, Jianwei Nai, Tiefeng Liu, Wenkui Zhang, Yujing Liu,* and Xinyong Tao*

The application of solid polymer electrolytes (SPEs) is still inherently limited by the unstable lithium (Li)/electrolyte interface, despite the advantages of security, flexibility, and workability of SPEs. Herein, the Li/electrolyte interface is modified by introducing Li_2S additive to harvest stable all-solid-state lithium metal batteries (LMBs). Cryo-transmission electron microscopy (cryo-TEM) results demonstrate a mosaic interface between poly(ethylene oxide) (PEO) electrolytes and Li metal anodes, in which abundant crystalline grains of Li, Li_2O , LiOH , and Li_2CO_3 are randomly distributed. Besides, cryo-TEM visualization, combined with molecular dynamics simulations, reveals that the introduction of Li_2S accelerates the decomposition of $\text{N}(\text{CF}_3\text{SO}_2)_2^-$ and consequently promotes the formation of abundant LiF nanocrystals in the Li/PEO interface. The generated LiF is further verified to inhibit the breakage of C—O bonds in the polymer chains and prevents the continuous interface reaction between Li and PEO. Therefore, the all-solid-state LMBs with the LiF-enriched interface exhibit improved cycling capability and stability in a cell configuration with an ultralong lifespan over 1800 h. This work is believed to open up a new avenue for rational design of high-performance all-solid-state LMBs.

Lithium (Li) metal batteries (LMBs) have attracted increasing attention due to the high theoretical capacity (3860 mAh g^{-1}) and low electrochemical potential (-3.04 V) of metallic Li.^[1,2] Nevertheless, the large-scale application of LMBs is inherently inhibited by the uncontrollable growth of Li dendrite on Li anode.^[3,4] The typical issue is addressed through various strategies, for example, the interfacial SEI engineering,^[5,6] stable hosts construction,^[7,8] and solid electrolyte design.^[9,10] Among the strategies, the solid state electrolytes, particularly the solid polymer electrolytes (SPEs) for LMBs, have gained tremendous interest for many decades.^[9,11–13] A range of advantages from SPEs, including their satisfactory mechanical properties, high cathodic stability, inexpensive cost, low gravimetric density, and accessibility toward large-scale manufacturing process,^[14–19] make it a promising substitute for liquid electrolyte

which suffers from safety hazards such as leakage and combustion.^[1,2,20–23] Nevertheless, the large-scale application of SPEs in LMBs is still inevitably hindered because of the sluggish transport of Li ions and poor affinity of the Li/electrolyte interface.^[24–28]

Considering the ultrahigh reducibility of Li, serious parasitic reactions (e.g., Li reacts with poly(ethylene oxide) (PEO) to form Li_2O , C_2H_4 , and H_2) inevitably occur at the Li/PEO interface to harm the performances of batteries.^[29–32] Moreover, the Li/PEO interface may be continuously thickened during the battery operation originated from the repeated reactions between fresh SPE and Li (Figure 1a), resulting in large electrochemical impedance and uneven surface morphology.^[27,33,34] These evolutions at the Li/PEO interface will lead to evident capacity fading with the inferior cyclability.^[24,33,35] Tremendous strategies have been proposed to address the intrac-

table issues in the Li/PEO interface, including constructing 3D matrix for Li metal, designing artificial SEI layers, and fabricating the mechanically strong SPEs.^[36–39] Of note, LiF is found as an excellent interfacial component which possesses low Li ions diffusion barrier and superior electronic insulation, thus facilitating the Li ions transfer and homogeneous Li deposits in the batteries with liquid electrolyte.^[40–42] Similarly, to realize a uniform distribution, or even in situ generation of LiF where PEO interfaces Li (Figure 1b), would be a challenging but logically suitable way to address the interfacial issues.

Additionally, in order to reveal the mechanism of how LiF enhances the interfaces, characteristic techniques for visualizing the interfacial evolutions are highly desired. The atomic force microscopy (AFM), X-ray photoelectron spectroscopy (XPS), time-of-flight secondary-ion mass spectrometry (TOF-SIMS), and Auger electron spectroscopy (AES) have been demonstrated to image the phases distribution or reveal the chemical composition.^[43–48] However, to atomically visualize such chemically sensitive interfaces and correspondingly employing the underlying promotion strategy, is still in a blank. Recently, cryo-transmission electron microscopy (cryo-TEM) has enabled the atomic observation of sensitive Li metal and its interfacial structure in liquid electrolytes.^[5,49–51] This inspiring progress encourages the reasonable idea for visualizing the Li/PEO interface at atomic scale.

O. Sheng, J. Zheng, Z. Ju, C. Jin, Dr. Y. Wang, M. Chen, Dr. J. Nai, Dr. T. Liu, Prof. W. Zhang, Dr. Y. Liu, Prof. X. Tao
College of Materials Science and Engineering
Zhejiang University of Technology
Hangzhou 310014, P. R. China
E-mail: yujingliu@zjut.edu.cn; tao@zjut.edu.cn

The ORCID identification number(s) for the author(s) of this article can be found under <https://doi.org/10.1002/adma.202000223>.

DOI: 10.1002/adma.202000223

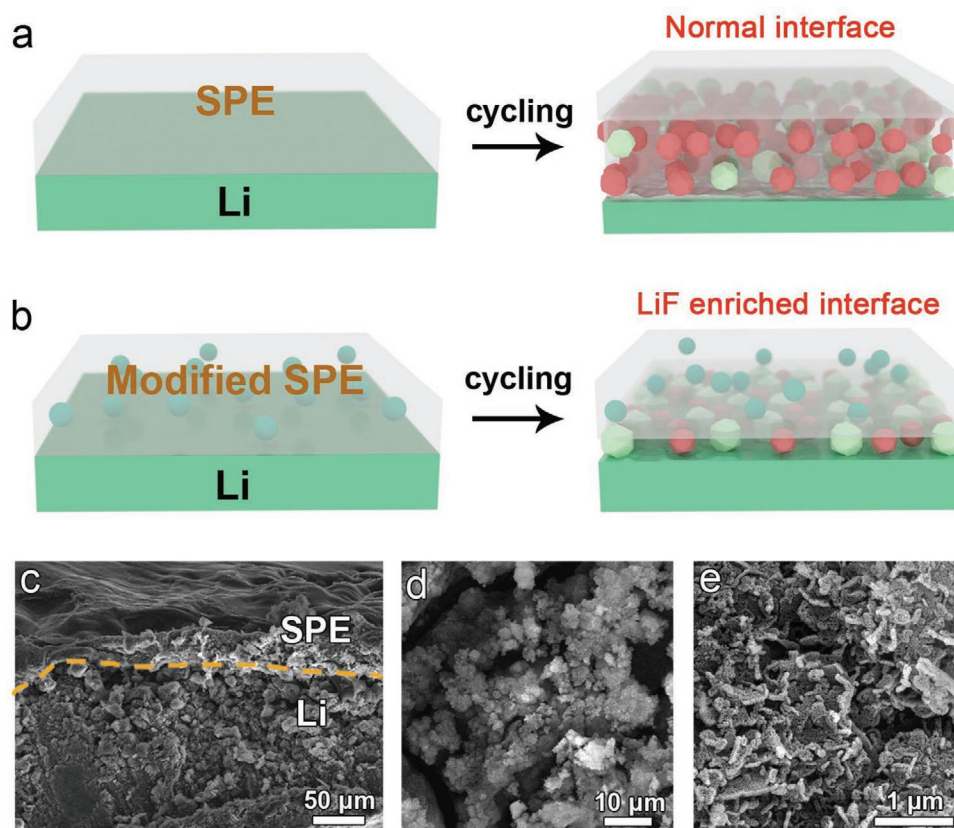


Figure 1. Illustration and morphology of the Li/PEO interface. a,b) Illustration of the different interfaces in pristine (a) and modified (b) SPEs during battery operation. c) Scanning electron microscopy (SEM) cross-section image of the Li/PEO interface after 250 cycles. d,e) The SEM images of the interface layer residue. The sample was prepared by uncovering the SPE layer in (c) and dropping it into acetonitrile to dissolve the SPE, and finally collecting the residue for SEM observation.

In this contribution, Li_2S is used as an additive of PEO based electrolyte. The atomic-resolution imaging from cryo-TEM declares a LiF-enriched interface when Li_2S is added into PEO. The in situ formation of uniform LiF nanocrystals at the interface, instead of mechanically blending insoluble LiF of aggregation, can effectively increase the diffusion properties and decrease the terrible reaction between Li metal and PEO, exemplifying the superiority of Li_2S additive. The underlying mechanism toward the formation of LiF induced by Li_2S and the suppression of parasitic reactions at Li/PEO interface is elucidated deeply. Through this interfacial design, the all-solid-state Li-LiFePO₄ and Li-LiNi_{0.8}Co_{0.1}Mn_{0.1}O₂ (NCM811) full cells exhibit stable cycling capability and rate properties. As such, this work has implications for the construction of stable all-solid-state LMBs with prolonged lifespan.

The morphologies of the normal Li/PEO interface are characterized and shown in Figure 1c–e. The cross-sectional image clearly shows many fine particles in the interface that may be the by-product of parasitic reactions between Li and PEO (Figure 1c). The top-view morphology of this interface was further observed by separating the Li metal and dissolving the SPE using acetonitrile, where abundant insoluble nanoparticles resulting from serious side reactions between Li and PEO were also found in the surface (Figure 1d,e). The phenomenon that only SPE was dissolved in acetonitrile and other side reaction

products were not dissolved is shown in Figure S1, Supporting Information. Such an unstable Li/PEO interface is greatly responsible for the inferior electrochemical performance and rapid battery failure.

Then, we conducted Li–Li symmetric cells to investigate the positive effect of modified SPE on stabilizing interface and enhancing electrochemical performance (Figure 2a–c; Figure S2, Supporting Information). The cell with bare PEO-LiN(CF₃SO₂)₂ (LiTFSI) electrolyte exhibited voltage polarization of ≈ 105 mV during the first 300 h cycling and then the cell began to fade. In sharp contrast, the lifespan of cell with LiF or Li_2S modified PEO-LiTFSI electrolyte was greatly increased. And the cell involving Li_2S exhibited longer lifespan with lower overpotential compared with the cell that involved LiF (Figure S2, Supporting Information). This phenomenon is attributed to the poor solubility of LiF inside the acetonitrile solvent and the consequent inhomogeneous interface of Li/PEO. As evidence, the LiF-modified electrolyte had a small amount of agglomeration, while the Li_2S -enhanced electrolyte had a more uniform surface morphology before cycling (Figure S4, Supporting Information). Especially, the cell using PEO-LiTFSI electrolyte with 1% Li_2S additive had a reduced voltage polarization of about 50 mV and delivered obviously improved cycling life of over 1800 h without the remarkable increase of overpotential (Figure 2a–c). This lifespan has exceeded the results of various SPEs reported

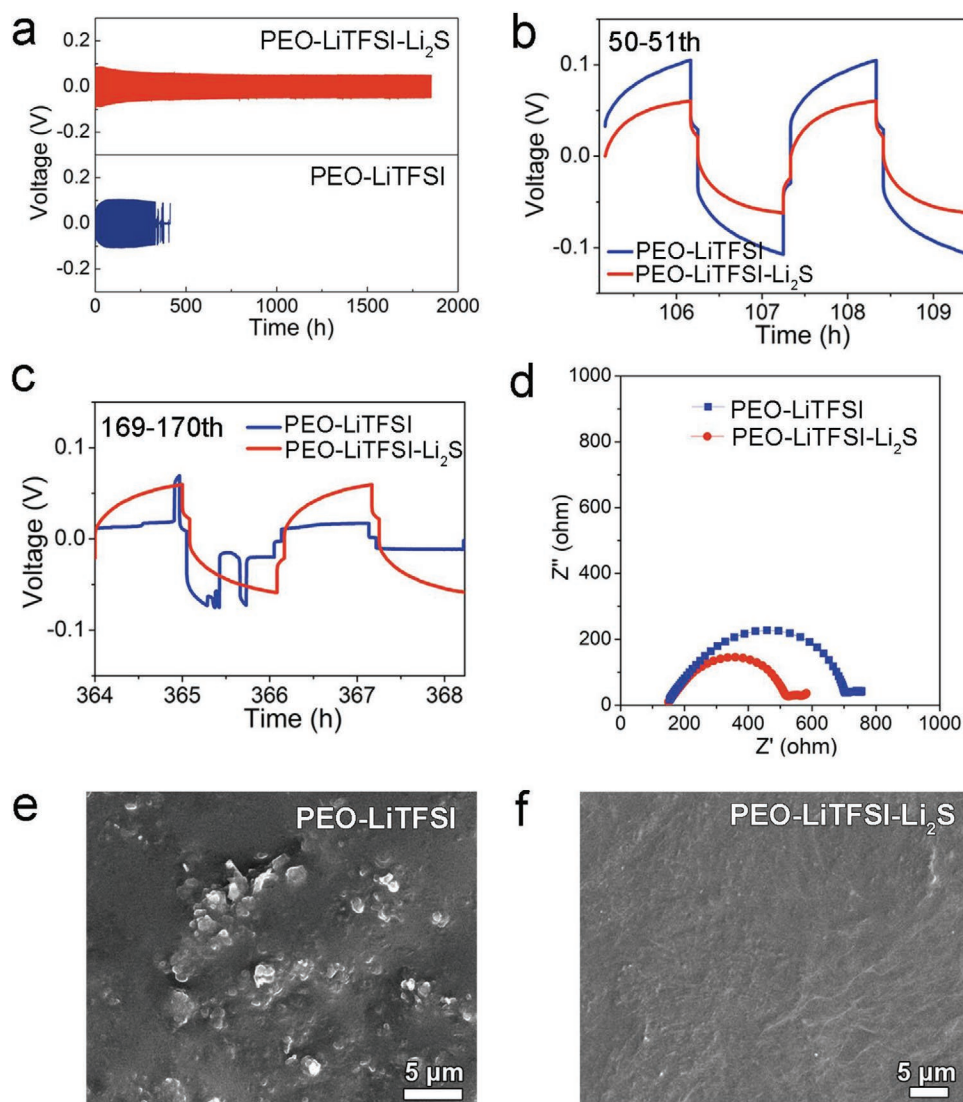


Figure 2. Electrochemical properties and morphology of the PEO-LiTFSI and PEO-LiTFSI-Li₂S electrolytes. a) Galvanostatic cycling performance of Li-Li symmetric cells at 50 °C (0.1 mA cm⁻²). b, c) Enlarged voltage profile of Li symmetric cells: b) 50–51 cycles, c) 169–170 cycles. d) Electrochemical impedance spectroscopy (EIS) spectra of Li-Li symmetric cells employing different SPEs. e, f) SEM images of the SPEs surface after 250 cycles.

in most of the literatures (Table S1, Supporting Information). Moreover, the fresh Li-Li cell using PEO-LiTFSI electrolyte has an impedance of 557 Ω (Figure 2d), significantly higher than the Li₂S modified cell (374 Ω). When further observing the morphologies of the Li surface after cycling for 50, 150, 250, and 300 cycles (Figure S6, Supporting Information), we found that the Li surface interfacing PEO-LiTFSI electrolyte gradually deteriorated as the cycling increased. The surface was covered with small bumps and sharp particles, which aggregated and were embedded inside the SPE after 250 cycles (Figure 2e). Conversely, the Li₂S modified electrolytes contributed to smooth, flat Li and SPE surface after as long as 300 cycles (Figure 2f; Figure S6, Supporting Information). Besides, C, O, S, and F elements uniformly distributed on the surface of both the PEO-LiTFSI (Figure S7, Supporting Information) and PEO-LiTFSI-Li₂S electrolyte (Figure S8, Supporting Information), indicates that the particles adhered on SPE in Figure 2e should be dead

Li and/or metallic Li relics after cycling. All these reveal the significant effect of Li₂S on enhancing the Li/PEO interfacial stability.

We also found that the introduction of Li₂S enhanced the ionic conductivity of SPE (Figure S9a, Supporting Information). The improvement of ionic conductivity by Li₂S additive can be attributed to the increase of Li ion transference number (t_{Li^+}) and Li ion mobility.^[36] After the addition of Li₂S, t_{Li^+} increased from 0.21 to 0.40 (Figure S10, Supporting Information), which may originate from the promoted Li ion dissociation from LiTFSI (Figure S11, Supporting Information). In addition, the decrease of melting transition temperature after the Li₂S introduction indicates the reduction of polymer crystallinity and the consequent increase of segmental motion (Figure S9b, Supporting Information), which can also boost the Li ion mobility. All these factors contribute to the enhancement of ionic conductivity.

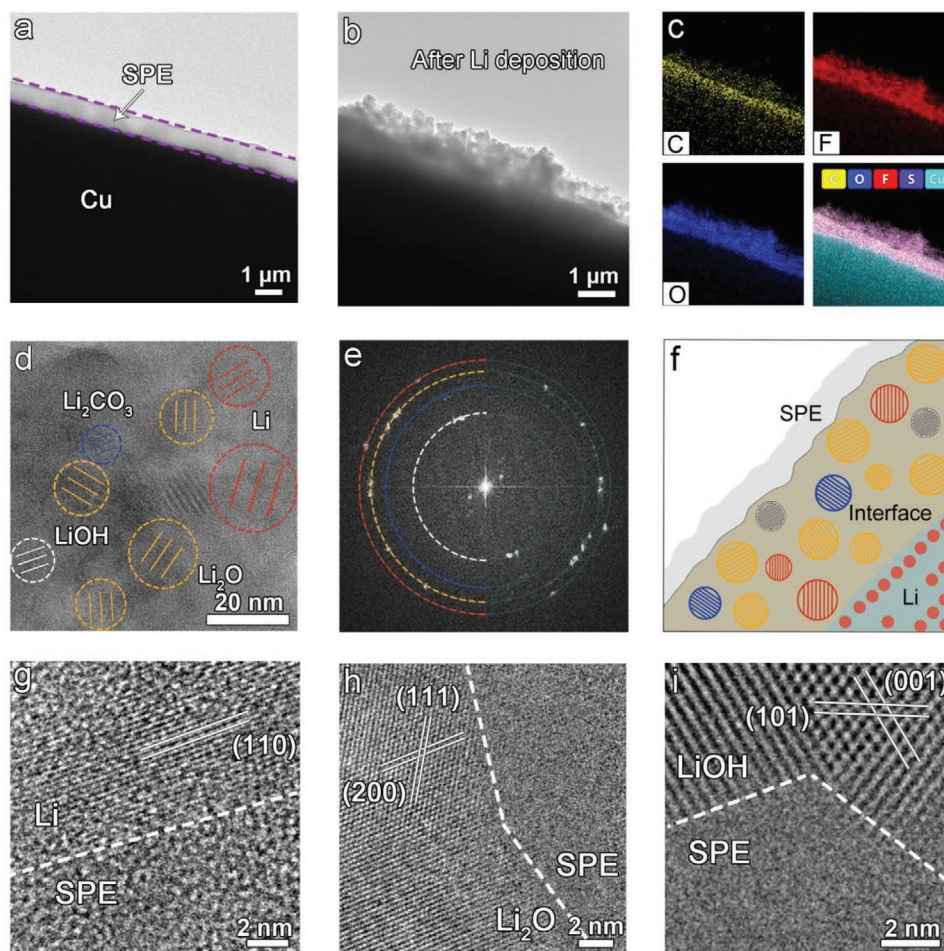


Figure 3. Cryo-TEM characterization of Li/PEO interface using PEO-LiTFSI electrolyte. a,b) TEM images illustrating morphological change before and after Li deposition. The layer between the purple lines is identified as the SPE. c) The corresponding distributions of C, O, F, S, and Cu elements. d) Recognized crystalline grains of Li metal, Li_2O , Li_2CO_3 , and LiOH in interface. e) The corresponding FFT of (d), red circle: Li, 2.48 Å, yellow circle: Li_2O , 2.66 Å, blue circle: Li_2CO_3 , 3.02 Å, white circle: LiOH, 4.35 Å. f) Schematic diagram for the identified mosaic structure of interface. g–i) HRTEM images of the interface between crystalline Li, Li_2O , and LiOH, and amorphous SPE.

To further understand the underlying reasons for the failure of pristine Li/PEO interface, we observed the morphology and composition of interface at the atomic level under assistance of cryo-TEM. The process of sample preparation using Cu-LiFePO₄ cell is shown in Figure S12, Supporting Information. First, the SPE layer with the thickness of $\approx 1\ \mu\text{m}$ was uniformly coated on the surface of the Cu grid (Figure 3a). The Cu grid provided the electron pathway and SPE supplied the ion conduction channel for Li deposition. After depositing Li at the corresponding position (Figure 3b), large bulk Li existed between the SPE and Cu grid, partially pushing up the flexible SPE. And the deposited Li in all-solid-state LMBs was neither dendritic nor spherical, but irregular bulk. Additionally, the SPE turned into heterogeneously porous, which is probably derived from the unwilling reaction with Li (Figure 3b). The STEM mappings in Figure 3c clearly demonstrate the distribution of concentrated C, F, O, and S elements in the interface layer. Moreover, the enlarged interface had both crystalline and amorphous areas that were composed of Li metal, LiOH, Li_2O , Li_2CO_3 , and SPE (Figure 3d). The fast Fourier transform (FFT) corresponding to Figure 3d

reconfirmed the existence of the inorganic Li compounds and Li metal (Figure 3e). Noticeably, the Li metal approaching PEO existed as polycrystalline particles rather than the single crystalline Li found in the batteries with liquid electrolyte,^[49] which was further clearly revealed by the selected area electron diffraction (SAED) (Figure S13, Supporting Information). The corresponding schematic diagram for the observed mosaic structure of interface is shown in Figure 3f.

We next captured high-resolution TEM (HRTEM) images to study the specific nanostructure of the interface (Figure 3g–i). In Figure 3g, the calibrated interplanar spacings of 2.48 Å match well with the (110) plane of metallic Li. Similarly, in Figure 3h,i, the crystalline Li_2O and LiOH with lattice aligning along (111) (200) and (101) (001) can be seen, respectively. Besides, the major area of the interface layer was amorphous, which may be composed of SPE. As such, we identified the Li/PEO interface as a mosaic model involving crystalline grains and amorphous phase. This result is consistent with the simulations that Li_2O would be generated at Li/PEO interface and partially supports the prediction of the distribution of various Li

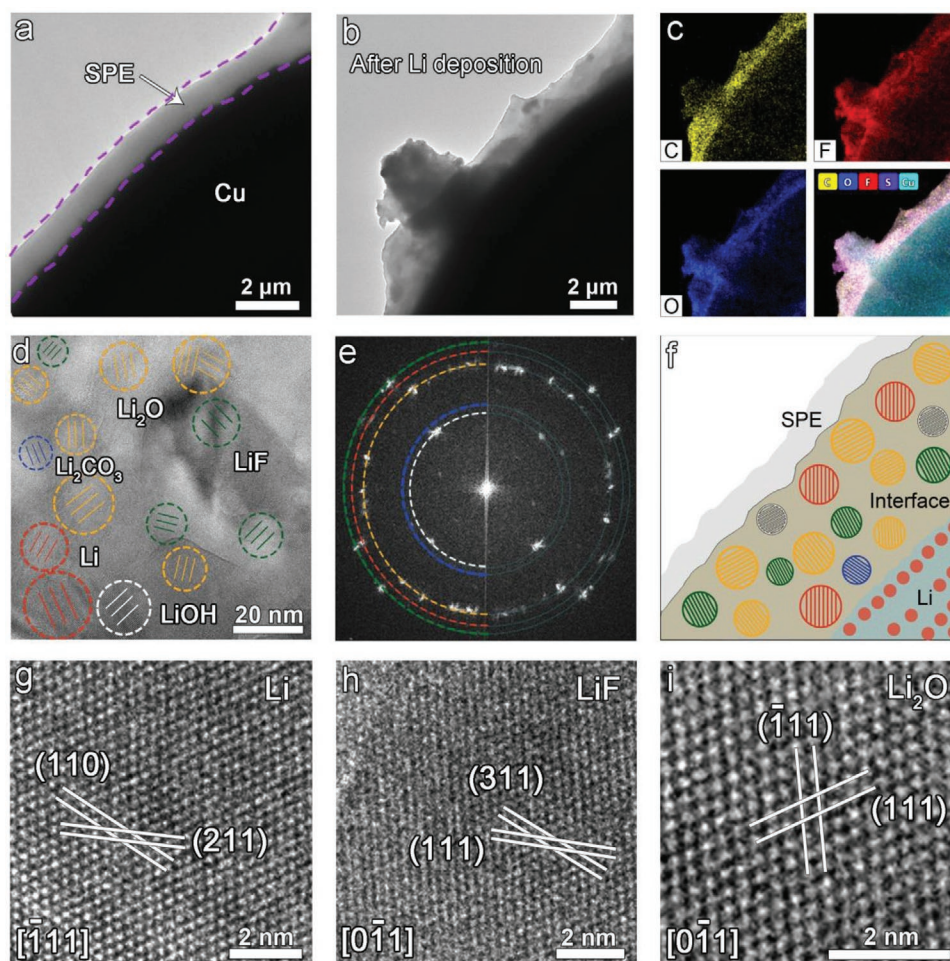


Figure 4. Cryo-TEM characterization of Li/PEO interface using PEO-LiTFSI-Li₂S electrolyte. a,b) TEM images illustrating morphological change before and after Li deposition. The layer between the purple lines is identified as the SPE. c) The corresponding distributions of C, O, F, S, and Cu elements. d) HRTEM image of the interface where the typical interfacial mosaic morphology and crystalline regions are showed. e) The corresponding FFT of (d), green circle: LiF, 2.32 Å, red circle: Li, 2.48 Å, yellow circle: Li₂O, 2.66 Å, blue circle: Li₂CO₃, 4.16 Å, white circle: LiOH, 4.35 Å. f) Schematic diagram of the observed LiF-rich interface. g–i) HRTEM images of Li, LiF, and Li₂O showing long-range ordering lattice.

compounds inside interfacial structure.^[29,43] Particularly, we demonstrate that the crystalline Li particles are also incorporated in the interface apart from Li compound crystals.

Furthermore, the Li₂S-participated interfacial evolution was detected by cryo-TEM. **Figure 4a,b** shows the morphology changes of SPE layer before and after Li depositing on the same position. The Li metal grew into some bulks coated with SPE and the SPE remained intact with Li, indicating the possible effects of Li₂S additive on hindering the continuous reaction between Li and PEO. The elemental mappings of C, O, S, and F inside the region where Li interfaced PEO-LiTFSI-Li₂S also reveal the distribution of different phases (Figure 4c). TEM image with higher magnification identified the mosaic structure of the interface that consisted of amorphous phase and embedding Li, Li₂O, LiOH, Li₂CO₃, and LiF nanocrystals (Figure 4d), which are further confirmed by the FFT in Figure 4e. The corresponding schematic diagram for the observed LiF-rich interface is shown in Figure 4f.

Particularly, the indexed crystal structures of the crystalline Li metal, LiF, and Li₂O are clearly presented in Figure 4g–i.

Observations at other locations in Figure S14, Supporting Information, also confirm the similar interface components. Furthermore, in-depth XPS verified that the surface layer was composed of SPE, Li metal, LiF, and Li₂O while the bottom layer on deposited Li was mainly consisted of Li, LiF, and Li₂O (Figures S15 and S16, Supporting Information), which were consistent with cryo-TEM results. Of note, the SPE modified by Li₂S shows the LiF-enriched interface, which is quite different from PEO-LiTFSI electrolyte. This may be the main reason for the interface improvement that prevents the side reaction between Li and PEO, meanwhile accelerating the ion diffusion in the interface layer.

In order to reconfirm the distribution of different components in Li/PEO interface, the SnapMap imaging test in XPS was further employed (**Figure 5a**). In turn from bottom to top, it can be seen that Li element was mainly distributed in the bottom layer. On basis of the line scanning from bottom to top (Figure S17, Supporting Information), we found the F content in the interface layer improved remarkably. Then we performed mass content analysis for points 1–3 in Figure 5a, where F

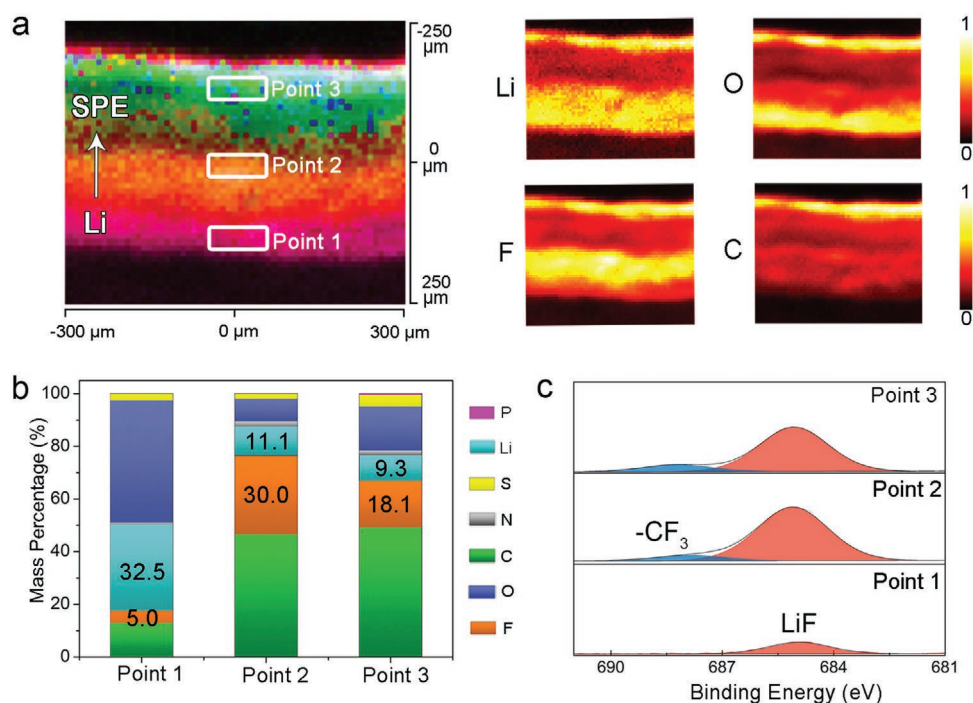


Figure 5. Distribution of various chemical constituents in interface. a) SnapMaps imaging test in XPS of each Li, F, O, and C element at the Li, PEO-LiTFSI-Li₂S electrolyte, and interface layer. b) The mass content of each element in the points 1–3. c) XPS spectra of F element in the point 1–3, F 1s.

content at point 2 was close to 30%, significantly higher than point 1 (5%) and point 3 (18.1%) (Figure 5b). Particularly, Figure 5c and Figures S18 and S19, Supporting Information, show that the concentrated F element mainly originates from inorganic LiF, and the content of LiF at point 2 was 27.2%.

As the N(CF₃SO₂)₂[−] (TFSI[−]) ionic group is the only source for producing LiF, it is assumed whether Li₂S could affect the TFSI[−] decomposition kinetics. AIMD simulations were used to confirm this conjecture (Figure 6a,b; Figure S21, Supporting Information). The optimized atomic positions of the simulated model were determined by the intermolecular interaction between LiTFSI and Li₂S, as well as the orientation of LiTFSI absorbed on the Li metal surface (Figure S20, Supporting Information). Figure 6b shows the TFSI[−] decomposition sequences when the PEO-LiTFSI-Li₂S electrolyte was situated close to the Li surface. In this case, the TFSI[−] was reduced and a C–S bond breaks within 40 fs, becoming CF₃[−] and CF₃SO₂NSO₂^{2−}. The CF₃[−] further decomposes into its constituents F and CF₂ in the next 210 fs, while the CF₃SO₂NSO₂^{2−} remains unchanged. Besides, another C–F bond break occurs at 600 fs. As for the PEO-LiTFSI electrolyte, the C–S bond break occurs within 250 fs and CF₃[−] further decomposes into F and CF₂ at 600 fs (Figure 6a), which clearly indicates that Li₂S accelerates the chain breaking of C–S and C–F bonds. Furthermore, the bond dissociation energy (ΔE) required for the TFSI[−] to decompose into F ion were calculated by density functional theory (DFT). When Li₂S exists in the SPE, the required ΔE (5.24 eV) is much lower compared with PEO-LiTFSI electrolyte of 6.81 eV (Figure S22, Supporting Information). Hence, the simulations systematically prove that Li₂S promotes the decomposition of Li salts to in situ produce LiF, which well illustrates the findings of LiF in both the cryo-TEM and XPS results. Importantly, as seen in

Figure 6c,d, the C 1s signals of pristine SPE had a sharp decline of C–O configuration after cycling attributed to the undesirable parasitic reactions between Li and PEO. In sharp contrast, the SPE with Li₂S additive showed no obvious reduction in C–O bonds, which further indicates that the uniform distribution of LiF nanocrystals in interface can inhibit the reaction of Li and PEO.

As the chemical stability of SPE was effectively improved and a stable LiF-rich interface was harvested, which could further contribute to enhance the electrochemical stability and suppress the formation of Li dendrites, we used PEO-LiTFSI-Li₂S electrolyte to assemble all-solid-state LMBs. Figure 7a presented the initial discharge/charge curves of LiNi_{0.8}Co_{0.1}Mn_{0.1}O₂ (NCM 811)/electrolyte/Li batteries in the voltage range of 2.7–4.2 V. The initial specific charge capacity of PEO-LiTFSI-Li₂S and PEO-LiTFSI electrolyte based batteries were around 257 and 153 mAh g^{−1}, respectively. In Figure 7b, the PEO-LiTFSI-Li₂S also delivered excellent cycling stability and high coulombic efficiency near 100% at 0.2 C for over 150 cycles. And the capacity retention after 150 cycles was 91.2%, which was much higher than PEO-LiTFSI batteries (57.3%, 100 cycles). The configuration of PEO and NCM 811 in this work has rarely been reported in literatures. Of note, such a combination delivers much better cyclability even than most of NCM 532/PEO systems at present.^[52] Moreover, in Figure S26, Supporting Information, the charge-transfer resistance (R_{ct}) at the interface of batteries with PEO-LiTFSI-Li₂S electrolyte was 122 Ω , which was smaller than PEO-LiTFSI electrolyte (274 Ω). Besides, the electrochemical performance of LiFePO₄/Li cell was also evaluated. Figure S27, Supporting Information, shows that the discharge/charge plateaus of LiFePO₄/Li cells were around 3.35 and 3.50 V at 0.3 C. The cycling performance is shown in Figure S28, Supporting

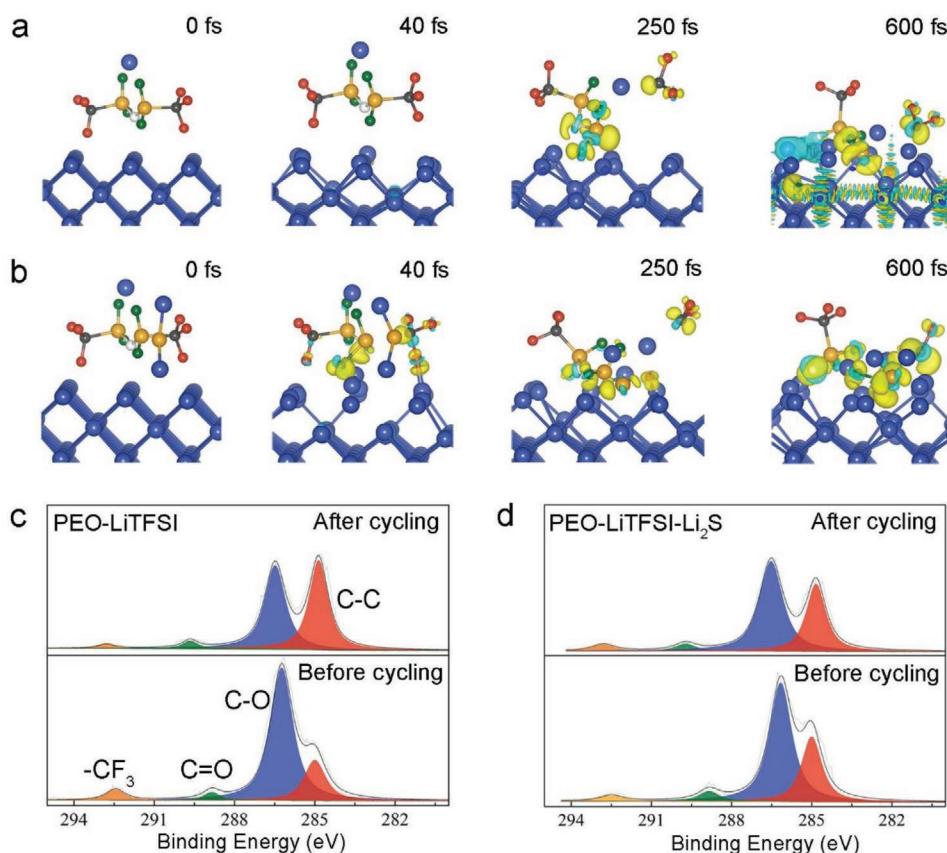


Figure 6. The simulation depicting LiF formation induced by Li₂S and XPS characterization. a,b) Sequences of TFSI⁻ decomposition obtained from AIMD simulations for PEO-LiTFSI electrolyte (a) and PEO-LiTFSI-Li₂S electrolyte (b). The TFSI⁻ was assumed adjacently to the Li surface at 0, 40, 250, and 600 fs. c,d) XPS characterization of SPE before and after cycles of PEO-LiTFSI electrolyte (c) and PEO-LiTFSI-Li₂S electrolyte (d).

Information. When the battery with PEO-LiTFSI-Li₂S electrolyte was cycled at 0.5 C (Figure 7c), the specific capacity of LiFePO₄-Li cell was 140 mAh g⁻¹. Meanwhile, the PEO-LiTFSI-Li₂S enabled battery also delivered a more stable coulombic efficiency of 99%, and the capacity retention after 1000 cycles showed a value of 85%, which was much higher than PEO-LiTFSI batteries (77% for 150 cycles), demonstrating the ultrastable interface established by the F-rich interface. The capacity increase of the first 15 cycles was related to the wetting process between the electrode and SPE interface.^[53] The first coulombic efficiency was less than 90% when using PEO-LiTFSI-Li₂S electrolyte, which was mainly attributed to two reasons: 1) Li consumption and SPE decomposition during the formation of SEI in the initial cycles,^[54] 2) the side reaction of the Li₂S redox transition into Li₂S_x ($x > 2$).^[55,56] Figure 7d compared the rate performance of all-solid-state LMBs. The specific capacity of battery with PEO-LiTFSI-Li₂S electrolyte was 156, 149, 125, 114, and 83 mAh g⁻¹ at 0.2, 0.4, 0.8, 1.0, and 2.0 C, respectively. When the current density returned to 0.4 C, the discharge capacity could reach back to 146 mAh g⁻¹. In contrast, the specific capacity of battery with PEO-LiTFSI electrolyte was only 140, 132, 100, 85, and 31 mAh g⁻¹ at 0.2, 0.4, 0.8, 1.0, and 2.0 C, respectively. The capacity at a higher rate was higher in PEO-LiTFSI-Li₂S compared to PEO-LiTFSI, which was due to the presence of Li₂S that can help form a stable LiF-rich SEI to promote more dense

and smooth Li deposition, increase the amount of transportable Li⁺, allow efficient transport of Li⁺, and enable uniform Li deposition.^[54,57]

When we further tracked the impedance after different cycles, the R_{ct} at the interface for battery with PEO-LiTFSI electrolyte (Figure 7e) showed non-linear changes, but generally increased after prolonged cycles (290, 240, 250, 340, and 350 Ω after 10, 30, 70, 100, and 150 cycles, respectively). The increase in R_{ct} is due to possible side reactions at the interface that destroy the Li metal and SPE, and lead to the formation of unstable SEI.^[41,58,59] When Li₂S existed in the SPE, the R_{ct} was smaller than that of the pure PEO-LiTFSI electrolyte both before and after circulation, which originated from the improved solid-solid interfacial contact, the effective control of side reactions, and the stabilized LiF-rich SEI.^[60,61] In addition, the R_{ct} of PEO-LiTFSI-Li₂S batteries gradually increased in the initial cycles (190 Ω for 10 cycles) and declined in the following cycles (Figure 7f). The increase of R_{ct} after 10 cycles may be related to the adverse interface reactions for the initial generation of SEI. The following decrease of R_{ct} can be contributed to high ion conductivity, low diffusion barrier, and high surface energy of LiF-rich interface, which can allow sufficient Li⁺ transport and decrease the R_{ct} .^[58,62,63] In general, the strategy of introducing Li₂S can effectively engineer the stable interface and boost the performance of electrochemical operation. The

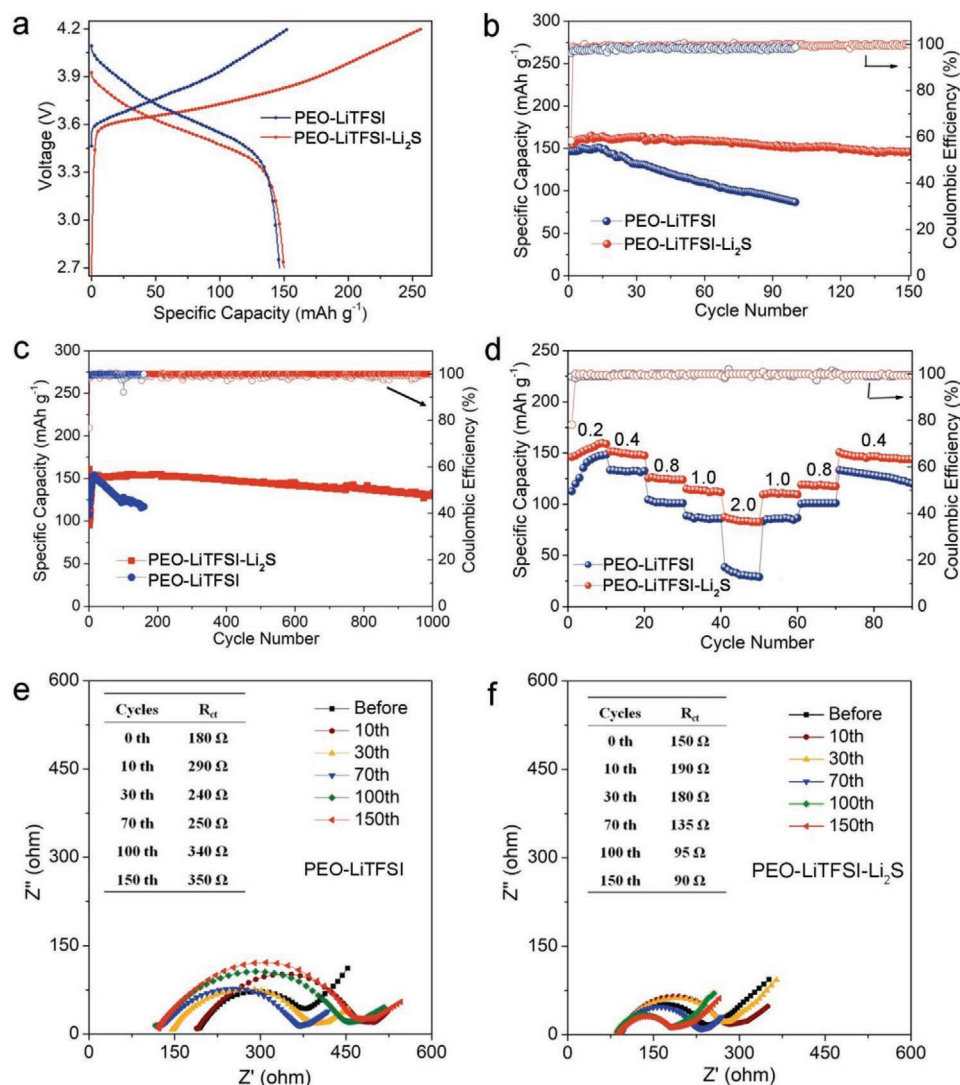


Figure 7. Electrochemical performance of all-solid-state LMBs with the PEO-LiTFSI-Li₂S and PEO-LiTFSI electrolyte at 50 °C. a) Typical charge and discharge profiles using NCM 811 cathode at first cycle, 2.7–4.2 V. b) Cycling performance of batteries using NCM 811 cathode at 0.2 C. c) Cycling performance of batteries using LiFePO₄ cathode at 0.5 C. d) Rate performance of batteries using LiFePO₄ cathode at 0.2, 0.4, 0.8, 1.0, and 2.0 C. e, f) EIS spectra of different batteries using LiFePO₄ cathode before cycling and after 10, 30, 70, 100, and 150 cycles.

obviously improved performances of PEO-LiTFSI-Li₂S based battery were attributed to the favorable interfacial stability of Li/PEO in battery.

In summary, the Li/PEO interface is clearly presented at atomic scale as the mosaic structure where Li, LiOH, Li₂O, and Li₂CO₃ nanocrystals are randomly distributed inside the amorphous phase (polymeric Li compounds or SPE possibly). The introduction of Li₂S inside SPE can promote the enrichment of LiF nanocrystals at the interface, which was confirmed by cryo-TEM and XPS. Particularly, the AIMD simulations and DFT results claimed that Li₂S can accelerate the decomposition of TFSI⁻ into LiF. Further analysis showed that LiF nanocrystals can effectively increase the ion diffusion properties, inhibit the chain breakage of C–O bond and prevent the continuous side reaction between PEO and Li metal. Benefiting from such interfacial design, both half- and full-cell with the optimized SPE deliver excellent electrochemical performance. This work

has accordingly provided the fundamental implications for constructing stable interface as well as high performance all-solid-state LMBs.

Supporting Information

Supporting Information is available from the Wiley Online Library or from the author.

Acknowledgements

The authors acknowledge financial support by the National Natural Science Foundation of China (Grant no. 51722210, 51972285, U1802254, and 21902144), and the Natural Science Foundation of Zhejiang Province (Grant no. LY17E020010, LD18E020003, and LQ20E030012). The authors acknowledge high-performance computational resources (TianHe-2) provided by LvLiang Cloud Computing Center of China.

Conflict of Interest

The authors declare no conflict of interest.

Keywords

cryo-transmission electron microscopy, interfaces, lithium metal anodes, polymer electrolytes

Received: January 10, 2020

Revised: June 14, 2020

Published online:

- [1] C. Jin, O. Sheng, J. Luo, H. Yuan, C. Fang, W. Zhang, H. Huang, Y. Gan, Y. Xia, C. Liang, J. Zhang, X. Tao, *Nano Energy* **2017**, 37, 177.
- [2] C. Jin, O. Sheng, Y. Lu, J. Luo, H. Yuan, W. Zhang, H. Huang, Y. Gan, Y. Xia, C. Liang, J. Zhang, X. Tao, *Nano Energy* **2018**, 45, 203.
- [3] H. Yuan, J. Nai, H. Tian, Z. Ju, W. Zhang, Y. Liu, X. Tao, X. W. D. Lou, *Sci. Adv.* **2020**, 6, eaaz3112.
- [4] D. Lin, Y. Liu, Y. Cui, *Nat. Nanotechnol.* **2017**, 12, 194.
- [5] Y. Gao, Z. Yan, J. L. Gray, X. He, D. Wang, T. Chen, Q. Huang, Y. C. Li, H. Wang, S. H. Kim, T. E. Mallouk, D. Wang, *Nat. Mater.* **2019**, 18, 384.
- [6] Z. Ju, J. Nai, Y. Wang, T. Liu, J. Zheng, H. Yuan, O. Sheng, C. Jin, W. Zhang, Z. Jin, H. Tian, Y. Liu, X. Tao, *Nat. Commun.* **2020**, 11, 488.
- [7] C. P. Yang, Y. X. Yin, S. F. Zhang, N. W. Li, Y. G. Guo, *Nat. Commun.* **2015**, 6, 8058.
- [8] Z. Liang, D. Lin, J. Zhao, Z. Lu, Y. Liu, C. Liu, Y. Lu, H. Wang, K. Yan, X. Tao, Y. Cui, *Proc. Natl. Acad. Sci. USA* **2016**, 113, 2862.
- [9] H. Zhang, X. Judez, A. Santiago, M. Martinez-Ibañez, M. Á. Muñoz-Márquez, J. Carrasco, C. Li, G. G. Eshetu, M. Armand, *Adv. Energy Mater.* **2019**, 9, 1900763.
- [10] W. Luo, Y. Gong, Y. Zhu, Y. Li, Y. Yao, Y. Zhang, K. K. Fu, G. Pastel, C.-F. Lin, Y. Mo, E. D. Wachsman, L. Hu, *Adv. Mater.* **2017**, 29, 1606042.
- [11] W. Liu, S. W. Lee, D. Lin, F. Shi, S. Wang, A. D. Sendek, Y. Cui, *Nat. Energy* **2017**, 2, 17035.
- [12] X. Chen, W. He, L. Ding, S. Wang, H. Wang, *Energy Environ. Sci.* **2019**, 12, 938.
- [13] D. Dong, B. Zhou, Y. Sun, H. Zhang, G. Zhong, Q. Dong, F. Fu, H. Qian, Z. Lin, D. Lu, Y. Shen, J. Wu, L. Chen, H. Chen, *Nano Lett.* **2019**, 19, 2343.
- [14] O. Sheng, C. Jin, J. Luo, H. Yuan, C. Fang, H. Huang, Y. Gan, J. Zhang, Y. Xia, C. Liang, W. Zhang, X. Tao, *J. Mater. Chem. A* **2017**, 5, 12934.
- [15] H. Zhang, U. Oteo, H. J. Zhu, X. Judez, M. Martinez-Ibañez, I. Aldalur, E. Sanchez-Diez, C. M. Li, J. Carrasco, M. Forsyth, M. Armand, *Angew. Chem., Int. Ed.* **2019**, 58, 7829.
- [16] D. G. Mackanic, W. Michaels, M. Lee, D. Feng, J. Lopez, J. Qin, Y. Cui, Z. Bao, *Adv. Energy Mater.* **2018**, 6, 1800703.
- [17] L. Wang, Y. Ye, N. Chen, Y. Huang, L. Li, F. Wu, R. Chen, *Adv. Funct. Mater.* **2018**, 4, 1800919.
- [18] X. Zhang, T. Liu, S. Zhang, X. Huang, B. Xu, Y. Lin, B. Xu, L. Li, C. W. Nan, Y. Shen, *J. Am. Chem. Soc.* **2017**, 139, 13779.
- [19] K. Xu, *Chem. Rev.* **2004**, 104, 4303.
- [20] L. Fan, S. Wei, S. Li, Q. Li, Y. Lu, *Adv. Energy Mater.* **2018**, 8, 1702657.
- [21] D. Lei, K. Shi, H. Ye, Z. Wan, Y. Wang, L. Shen, B. Li, Q.-H. Yang, F. Kang, Y.-B. He, *Adv. Funct. Mater.* **2018**, 28, 1707570.
- [22] Z. Guo, T. Wang, H. Wei, Y. Long, C. Yang, D. Wang, J. Lang, K. Huang, N. Hussain, C. Song, B. Guan, B. Ge, Q. Zhang, H. Wu, *Angew. Chem., Int. Ed.* **2019**, 58, 12569.
- [23] H. Duan, M. Fan, W. P. Chen, J. Y. Li, P. F. Wang, W. P. Wang, J. L. Shi, Y. X. Yin, L. J. Wan, Y. G. Guo, *Adv. Mater.* **2019**, 31, 1807789.
- [24] Q. Yang, C. Li, *Energy Storage Mater.* **2018**, 14, 100.
- [25] Y. He, C. Lu, S. Liu, W. Zheng, J. Luo, *Adv. Energy Mater.* **2019**, 9, 1901810.
- [26] C. Yan, X. B. Cheng, Y. X. Yao, X. Shen, B. Q. Li, W. J. Li, R. Zhang, J. Q. Huang, H. Li, Q. Zhang, *Adv. Mater.* **2018**, 30, 1804461.
- [27] N. Wu, Y. R. Shi, S. Y. Lang, J. M. Zhou, J. Y. Liang, W. Wang, S. J. Tan, Y. X. Yin, R. Wen, Y. G. Guo, *Angew. Chem., Int. Ed.* **2019**, 58, 18146.
- [28] S. A. Pervez, M. A. Cambaz, V. Thangadurai, M. Fichtner, *ACS Appl. Mater. Interfaces* **2019**, 11, 22029.
- [29] A. Mirsakiyeva, M. Ebadi, C. M. Araujo, D. Brandell, P. Broqvist, J. Kullgren, *J. Phys. Chem. C* **2019**, 123, 22851.
- [30] M. Ebadi, C. Marchiori, J. Mindemark, D. Brandell, C. M. Araujo, *J. Mater. Chem. A* **2019**, 7, 8394.
- [31] M. Ebadi, L. T. Costa, C. M. Araujo, D. Brandell, *Electrochim. Acta* **2017**, 234, 43.
- [32] Q. Zhou, J. Ma, S. Dong, X. Li, G. Cui, *Adv. Mater.* **2019**, 31, 1902029.
- [33] C. Wang, T. Wang, L. Wang, Z. Hu, Z. Cui, J. Li, S. Dong, X. Zhou, G. Cui, *Adv. Sci.* **2019**, 6, 1901036.
- [34] X. Zhang, S. Wang, C. Xue, C. Xin, Y. Lin, Y. Shen, L. Li, C. W. Nan, *Adv. Mater.* **2019**, 31, 1806082.
- [35] J. Wu, Z. Rao, Z. Cheng, L. Yuan, Z. Li, Y. Huang, *Adv. Energy Mater.* **2019**, 9, 1902767.
- [36] O. Sheng, C. Jin, J. Luo, H. Yuan, H. Huang, Y. Gan, J. Zhang, Y. Xia, C. Liang, W. Zhang, X. Tao, *Nano Lett.* **2018**, 18, 3104.
- [37] S.-S. Chi, Y. Liu, N. Zhao, X. Guo, C.-W. Nan, L.-Z. Fan, *Energy Storage Mater.* **2019**, 17, 309.
- [38] G. G. Eshetu, X. Judez, C. Li, O. Bondarchuk, L. M. Rodriguez-Martinez, H. Zhang, M. Armand, *Angew. Chem., Int. Ed.* **2017**, 56, 15368.
- [39] G. G. Eshetu, X. Judez, C. Li, M. Martinez-Ibanez, I. Gracia, O. Bondarchuk, J. Carrasco, L. M. Rodriguez-Martinez, H. Zhang, M. Armand, *J. Am. Chem. Soc.* **2018**, 140, 9921.
- [40] Y. Ozhables, D. Gunceler, T. A. Arias, *arXiv:1504.05799*, **2015**.
- [41] S. Choudhury, L. A. Archer, *Adv. Electron. Mater.* **2016**, 2, 1500246.
- [42] X. Cao, X. Ren, L. Zou, M. H. Engelhard, W. Huang, H. Wang, B. E. Matthews, H. Lee, C. Niu, B. W. Arey, Y. Cui, C. Wang, J. Xiao, J. Liu, W. Xu, J.-G. Zhang, *Nat. Energy* **2019**, 4, 796.
- [43] H. Zhang, U. Oteo, X. Judez, G. G. Eshetu, M. Martinez-Ibañez, J. Carrasco, C. Li, M. Armand, *Joule* **2019**, 3, 1689.
- [44] L. Xu, S. Tang, Y. Cheng, K. Wang, J. Liang, C. Liu, Y.-C. Cao, F. Wei, L. Mai, *Joule* **2018**, 2, 1991.
- [45] B. Sun, C. Xu, J. Mindemark, T. Gustafsson, K. Edström, D. Brandell, *J. Mater. Chem. A* **2015**, 3, 13994.
- [46] X. Tao, Y. Liu, W. Liu, G. Zhou, J. Zhao, D. Lin, C. Zu, O. Sheng, W. Zhang, H. W. Lee, Y. Cui, *Nano Lett.* **2017**, 17, 2967.
- [47] S. Wang, H. Xu, W. Li, A. Dolocan, A. Manthiram, *J. Am. Chem. Soc.* **2018**, 140, 250.
- [48] Y.-X. Song, Y. Shi, J. Wan, S.-Y. Lang, X.-C. Hu, H.-J. Yan, B. Liu, Y.-G. Guo, R. Wen, L.-J. Wan, *Energy Environ. Sci.* **2019**, 12, 2496.
- [49] Y. Li, Y. Li, A. Pei, K. Yan, Y. Sun, C.-L. Wu, L.-M. Joubert, R. Chin, A. L. Koh, Y. Yu, J. Perrino, B. Butz, S. Chu, Y. Cui, *Science* **2017**, 358, 506.
- [50] C. Fang, J. Li, M. Zhang, Y. Zhang, F. Yang, J. Z. Lee, M. H. Lee, J. Alvarado, M. A. Schroeder, Y. Yang, B. Lu, N. Williams, M. Ceja, L. Yang, M. Cai, J. Gu, K. Xu, X. Wang, Y. S. Meng, *Nature* **2019**, 572, 511.
- [51] M. J. Zachman, Z. Tu, S. Choudhury, L. A. Archer, L. F. Kourkoutis, *Nature* **2018**, 560, 345.
- [52] M. Wetjen, G.-T. Kim, M. Joost, G. B. Appetecchi, M. Winter, S. Passerini, *J. Power Sources* **2014**, 246, 846.

- [53] H. Wu, J. Wang, Y. Zhao, X. Zhang, L. Xu, H. Liu, Y. Cui, Y. Cui, C. Li, *Sustainable Energy Fuels* **2019**, 3, 2642.
- [54] R. Pathak, K. Chen, A. Gurung, K. M. Reza, B. Bahrami, F. Wu, A. Chaudhary, N. Ghimire, B. Zhou, W. H. Zhang, Y. Zhou, Q. Qiao, *Adv. Energy Mater.* **2019**, 9, 1901486.
- [55] S. Liang, C. Liang, Y. Xia, H. Xu, H. Huang, X. Tao, Y. Gan, W. Zhang, *J. Power Sources* **2016**, 306, 200.
- [56] T. Liu, H. Hu, X. Ding, H. Yuan, C. Jin, J. Nai, Y. Liu, Y. Wang, Y. Wan, X. Tao, *Energy Storage Mater.* **2020**, 30, 346.
- [57] C. Zhang, S. Liu, G. Li, C. Zhang, X. Liu, J. Luo, *Adv. Mater.* **2018**, 30, 1801328.
- [58] R. Pathak, K. Chen, A. Gurung, K. M. Reza, B. Bahrami, J. Pokharel, A. Baniya, W. He, F. Wu, Y. Zhou, K. Xu, Q. Q. Qiao, *Nat. Commun.* **2020**, 11, 93.
- [59] Z. Tu, S. Choudhury, M. J. Zachman, S. Wei, K. Zhang, L. F. Kourkoutis, L. A. Archer, *Nat. Energy* **2018**, 3, 310.
- [60] D. Gunceler, K. Letchworth-Weaver, R. Sundararaman, K. A. Schwarz, T. A. Arias, *Modell. Simul. Mater. Sci. Eng.* **2013**, 21, 074005.
- [61] L. Ma, M. S. Kim, L. A. Archer, *Chem. Mater.* **2017**, 29, 4181.
- [62] Y. Lu, Z. Tu, L. A. Archer, *Nat. Mater.* **2014**, 13, 961.
- [63] Y. Yuan, F. Wu, Y. Bai, Y. Li, G. Chen, Z. Wang, C. Wu, *Energy Storage Mater.* **2019**, 16, 411.